ACS Catalysis

Research Article

pubs.acs.org/acscatalysis

Highly Active Nonpromoted Hydrotreating Catalysts through the Controlled Growth of a Supported Hexagonal WS_2 Phase

Thibault Alphazan,[†] Audrey Bonduelle-Skrzypczak,[†] Christèle Legens,[†] Anne-Sophie Gay,[†] Zoubeyr Boudene,[†] Maria Girleanu,[§] Ovidiu Ersen,[§] Christophe Copéret,*[,‡] and Pascal Raybaud*[,†]

[†]IFP Energies nouvelles, Rond-point de l'échangeur de Solaize, 69360 Solaize, France

[‡]Department of chemistry and Applied Biosciences, ETH Zürich, Vladimir Prelog Weg 2, CH-8093 Zürich, Switzerland

[§]IPCMS-UMR 7504, CNRS-Université de Strasbourg, 23 rue du Loess BP 43, 67034 Strasbourg cedex 2, France

Supporting Information

ABSTRACT: Highly active nonpromoted W-based hydrotreating catalysts are prepared through a molecular approach with a control of each step. This approach yields WS_2 crystallites exhibiting hexagonal 2D morphology, which have been characterized by combining XPS and HR HAADF-STEM techniques and ab initio molecular modeling. The first step is the impregnation of a well-defined precursor, $[W(OEt)_5]_2$, grafted onto partially dehydroxylated amorphous silica–alumina (ASA) and characterized at the molecular level by spectroscopic techniques (NMR and IR). The use of increasing amounts of W precursor reveals the formation of (i) a layer of tungsten surface species grafted on the surface and (ii) layers of more mobile adsorbed species loosely bonded to the surface. Sulfidation of these materials provides WS_2 supported on ASA, which shows unprecedented lower sulfidation temperatures down to ambient temperature and improved activity by comparison with conventional references (polyoxometalate route). In addition, these improved activities are explained not only by a better level of sulfidation but also by the 2D hexagonal-like morphology of WS_2 crystallites (revealed by HR HAADF-STEM), in contrast to a truncated triangle-like morphology for conventional samples. This molecular approach thus opens new avenues to understand and improve the performances of hydrotreating catalysts.

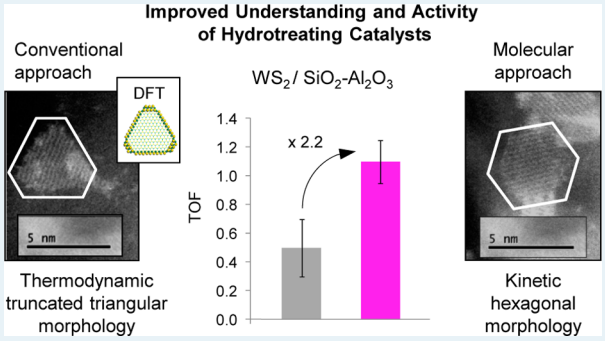

KEYWORDS: *WS_2, amorphous silica–alumina, hydrotreating catalyst, morphology, metallo-organic precursor, molecular approach, density functional theory*

INTRODUCTION

The evolution of oil world reserves and the stiffening of environmental regulations[1] call for a significant improvement of the performances of hydrotreating catalysts, which are used to remove O-, S-, and N-containing contaminants from petroleum.[2] These catalysts are mainly based on supported transition-metal sulfides (TMS).[3] The TMS active phase is usually composed of tungsten (W) or molybdenum (Mo), promoted by nickel (Ni) or cobalt (Co). It forms a bimetallic sulfide phase, typically called the NiWS, NiMoS, or CoMoS phase, whose structure corresponds to a two-dimensional (2D) nanolayer of $Mo(W)S_2$ decorated by the promoter at its edges.[4,5] The hydrogenation properties of MoS_2 and WS_2 phases, profitably used in the hydrotreatment (HDT) process, were recently highlighted by H_2/D_2 scrambling experiments.[6] While Ni-promoted WS_2 catalysts lead to activity improvement in aromatic hydrogenation,[7,8] optimizing the properties of WS_2-based catalysts remains a challenge, hence limiting their applications in HDT. One of the major problems is the difficulty in improving the level of sulfidation of the active phase due to the formation of $W(Mo)O_xS_y$ and amorphous $W(Mo)O_3$ inactive phases, probably as a result of the overly strong metal–support interactions.[9−11] The second challenge lies in the control of the morphology (bidimensional shape) and size of the WS_2 or MoS_2 nanocrystallites, observed either on model graphite supports,[2] or on industrial silica-alumina supports.[8] These challenges thus call for an improvement of synthetic methods with a full molecular control of the active phase.

Industrial MoS_2- and WS_2-based catalysts are conventionally prepared by a succession of steps with little control over the metal–support interaction: (i) an incipient wetness impregnation of aqueous solutions of W salts such as ammonium metatungstate onto an oxide support, typically alumina or silica–alumina, (ii) a drying and possibly a calcination step, and (iii) an activation step using a sulfo-reductive agent (such as dimethyl disulfide (DMDS) or an H_2S/H_2 gas mixture). The first step—impregnation—is critical because the deposition of

Received: September 2, 2014
Revised: October 20, 2014
Published: October 22, 2014

 © 2014 American Chemical Society dx.doi.org/10.1021/cs501311m | ACS Catal. 2014, 4, 4320−4331

the oxide precursor also affects the final activation step. During the impregnation of metal complexes on alumina, strong chemical interactions occur between the complex and the support.[9,10] They may be diminished by using chemical agents (citrate, phosphate).[11] In addition, as W(Mo) salts are heteropolyanions, thermal treatments of surface species are mandatory either before or during sulfidation, thus yielding less dispersed metal entities on the surface. This thermal treatment (calcination) can be detrimental to not only the number but also the "quality" of active sites (either lost in the support or in a refractory oxide phase). Furthermore, changing the nature of the support also modifies the size, morphology, and activity of the MoS_2 nanolayer[12,13] by altering the metal−support interaction. Regarding catalyst activation, this step is of primary importance to generate the highest amount of sulfide phase. However, the sulfidation level of the W phase according to X-ray photoelectron spectroscopy (XPS) still needs to be improved (by comparison with Mo) and requires high temperatures, which is also detrimental to dispersion. The lower sulfidation level of W thus represents a strong and longstanding unsolved limitation.[14−16]

Considering that the distribution of W entities on the surface and the intermolecular or intramolecular nature of their interactions greatly influence their transformation into WS_2 species, it is thus necessary to explore innovative synthetic routes beyond conventional methods, allowing a better control of each step. Thus, we explore the preparation of the active W phase with improved physicochemical and catalytic properties through the deposition of a well-defined W molecular precursor by impregnation on partially dehydroxylated ASA support followed by the sulfidation step. ASA is the support of choice in the hydrocracking (HCK) process; here it also provides hydroxyl groups[17] used as anchoring sites for W molecular complexes. The method of preparation used here is related to surface organometallic chemistry (SOMC), whose aim is to control the surface chemistry at surface of materials/supports to prepare well-defined fully characterized surface species using molecular precursors, typically organometallic reagents.[18−22] While SOMC has been successfully used to prepare well-defined single-site heterogeneous catalysts for many reactions, such as epoxidation,[23] hydrogenation,[24] polymerization (Zr,[25] Hf,[26] or Cr[27]), and alkene (Mo,[28] W,[29] or Re[30]) and alkane (W[31]) metathesis, this concept has been less frequently used for preparing TMS catalysts, since the pioneering work of Yermakov on NiWS.[32−38]

Here, we report the preparation of highly active unpromoted supported WS_2 catalysts through a molecular approach, referred to hereafter as controlled surface chemistry (CSC), which consists of (i) the deposition of a tungsten alkoxide precursor onto ASA, an industrial support, with a controlled hydroxyl density, followed by (ii) a sulfidation step. These materials are fully characterized at each step by a multitechnique approach (combining IR, NMR, XPS, TEM, HAADF-STEM, and DFT) and exhibit a high level of sulfidation and a WS_2 phase with a 2D hexagonal morphology. This specific morphology is a direct consequence of the mild bottom-up preparation method and provides improved catalytic activities in comparison with conventional catalysts.

EXPERIMENTAL METHODS

Preparation and Activation of ASA-Supported Materials. All experiments were carried out by using standard Schlenk and glovebox techniques. Solvents were purified and dried by a solvent purification system (SPS-M-Braun); they were degassed by freeze−pump−thaw cycles and stored over 4 Å molecular sieves under argon. $[W(OEt)_5]_2$ and $CH_3{}^{13}CH_2OH$ (99% ^{13}C labeled) were obtained from Alfa Aesar and Cortecnet, respectively. All chemical products were used as received. Ammonium metatungstate and amorphous ASA with 30 wt % SiO_2 were purchased from industrial partners.

Preparation and Characterization of ASA Partially Dehydroxylated at 300 °C, Denoted ASA_{300}. ASA samples (extrudates, 1 g, 229 $m^2\ g^{-1}$) were calcined for 6 h under air (static conditions), using a ramp of 5 °C min^{-1} up to 300 °C. Then, the solid was partially dehydroxylated at 300 °C under high vacuum (5×10^{-5} mbar) for ca. 16 h. The system was cooled to 140 °C using a ramp of 10 °C min^{-1}, and the extrudates were stored in a glovebox. After this treatment, the specific surface area was 228 $m^2\ g^{-1}$. The OH density was measured by titration by quantification of CH_4 evolved upon contacting ASA with CH_3MgBr (1.3 M) in diethyl ether. ASA_{300} presents a OH density of 1.22 mmol OH g^{-1}: i.e., 3.2 OH nm^{-2}.

Preparation of $[W(OEt)_5]_2$ Supported on ASA_{300} (0.2 W nm^{-2}) via Incipient Wetness Impregnation (IWI). Representative Procedure. After $[W(OEt)_5]_2$ (0.141 g, 0.34 mmol) was stirred in cyclohexane (1.92 mL) for 10 min, an aliquot of the solution (280 μL) was used to impregnate ASA_{300} extrudates (0.491 g). After a maturation step of 16 h in order to let the species diffuse into the ASA, the extrudates were dried under high vacuum (5×10^{-5} mbar) for 2 h to give an off-white solid referred as $[W(OEt)_5]_2$-IWI-/ASA_{300} (1.5 wt % W, ca. 0.2 W nm^{-2}), which was stored in the glovebox.

Following the representative procedure, impregnation solutions containing higher amounts of $[W(OEt)_5]_2$ precursor were used for IWI of ASA, affording material with W coverages of 0.5, 0.8, 1.7, and 3.7 W nm^{-2}, as reported in the Supporting Information. Note that, upon deposition, less than 0.1 EtOH (deposited W)$^{-1}$ was observed for W coverage below 1.7 W nm^{-2}, implying the formation of ethoxy surface species EtO_{ASA} or adsorption of EtOH. Preparation of carbon-13 labeled $[W(OEt^*)_5]_2$ precursor and related supported materials are also described in the Supporting Information.

Preparation of Supported WS_2 Catalysts: Sulfidation at 350 °C. Representative Procedure. In a sulfidation cell, the W-supported material $[W(OEt)_5]_2$-IWI-/ASA_{300} (ca. 2.0 g) was loaded under argon (glovebox). After connection and purge of the system with argon, the material was treated with a H_2S/H_2 mixture (15 mol % H_2S, 1×10^3 mbar) at a flow rate of 2 L (g of cat)$^{-1}$ h^{-1} and heated to 350 °C (sulfidation temperature), using a ramp of 5 °C min^{-1}. After 2 h at 350 °C, the cell was purged with argon (same flow rate and pressure) and the system was cooled first to 250 °C (12 °C min^{-1}). After 2 h at 250 °C, the system was further cooled to 120 °C (20 °C min^{-1}) and then evacuated for 5 min at ca. 1 mbar before being cooled to room temperature. The resulting sulfide material (black extrudates), denoted WS_2-IWI-/ASA_{300}-S350 (350 being the sulfidation temperature in °C) was directly stored in the glovebox or sealed in an ampule.

Sulfidation procedures used for temperatures such as −25, 0, 23, 150, and 250 °C are described in the Supporting Information.

Preparation of Conventional Catalysts. Incipient wetness impregnation of an aqueous solution of ammonium metatungstate on ASA followed by a maturation step of 16 h and subsequent drying at 120 °C (ca. 16 h) yielded so-called "dried"

dx.doi.org/10.1021/cs501311m | ACS Catal. 2014, 4, 4320−4331

materials, which could be further treated at 450 °C for 2 h in air at a flow rate of 1.5 L (g of cat)$^{-1}$ h^{-1} to give "calcined" material. Dried and calcined materials, with W coverages of 0.5, 1.8, and 3.7 W nm^{-2}, underwent sulfidation at between 23 and 600 °C using the procedures described above.

Characterization Techniques. TEM micrographs were obtained with a JEOL-2100F FEG transmission electron microscope operating at 200 kV. High-resolution scanning transmission electron microscopy (STEM) in high angle annular dark field (HAADF) experiments were performed on a JEOL 2100F TEM/STEM instrument operating at 200 kV, equipped with a Cs aberration probe corrector. X-ray photoelectron spectroscopy (XPS), FT-IR, and NMR analyses, as well as additional information, are detailed in the Supporting Information.

Catalytic Test. Catalytic activity measurements in toluene hydrogenation (HYD) were carried out in a Flowrence 16 fixed bed unit reactor from Avantium. Catalysts were presulfided ex situ prior to catalytic tests (according to conditions described hereafter) and loaded into reactors under argon. Then, catalysts underwent an activation step. A model feed composed of dimethyl disulfide (DMDS; 5.9 wt %), toluene (20 wt %), cyclohexane (73.6 wt %), and aniline (0.5 wt %) was injected from room temperature to 350 °C with a ramp of 2 °C min^{-1}. During the temperature increase, the liquid hourly space velocity (LHSV) was equal to 4 h^{-1} and the total pressure was 6 × 10^4 mbar. Then, the LHSV was lowered to 2 h^{-1}. The hydrogen to feed ratio (H_2/HC) was 450 NL L^{-1}. Note that DMDS decomposed into CH_4 and H_2S and that the partial pressure of H_2S maintained the sulfided state of the catalysts during the test. In order to measure a more accurate value of hydrogenation, catalysts were tested in the presence of aniline to inhibit the effect of mild acidity provided by ASA itself.[39] After 2 h at 350 °C, liquid products of the reaction were analyzed by gas chromatography. The hydrogenation rate was evaluated once the catalyst was stabilized. The intrinsic HYD rate is expressed in moles of toluene converted per moles of tungsten per hour (r_i). This rate can be normalized (r_i') per mole of tungsten incorporated in the WS_2 phase in spent catalysts (mol(W_{WS2}), as calculated from XPS and elemental analyses) in order to better reflect the activity of active slabs, since not all W atoms are sulfided.

Computational Methods. Total energies were calculated with plane wave density functional theory (DFT) within the generalized gradient approximation[40] and periodic boundary conditions. We used the Vienna ab initio simulation package[41] to solve the Kohn–Sham equations[42] within the projected augmented wave formalism.[43] All technical parameters and the method used to determine the morphology diagram of the WS_2 layers are detailed in the Supporting Information.

RESULTS

IR and Solid-State NMR Monitoring of [W(OEt)$_5$]$_2$ Deposition on ASA$_{300}$. ASA partially dehydroxylated at 300 °C under high vacuum (ASA_{300}) exhibiting W coverages of ca. 0.2, 0.5, 0.8, 1.7, and 3.7 W nm^{-2} were synthesized according to the protocol describes in Experimental Methods and the Supporting Information. As a preliminary remark, ASA_{300} presents an OH density of 3.2 OH nm^{-2}; this implies that we expect the formation of grafted species at low W coverage and additional adsorbed species as multilayers at higher coverage. In addition, since the projected area of [W(OEt)$_5$]$_2$ is ca. 1.0 nm^2, a maximum density of 2.0 W nm^{-2} is expected to be grafted on ASA.

In order to obtain molecular insight into the various grafted and adsorbed species, the impregnation process was monitored by IR and solid-state NMR spectroscopy. With increasing amounts of [W(OEt)$_5$]$_2$ impregnated on ASA_{300} (Figure 1), the

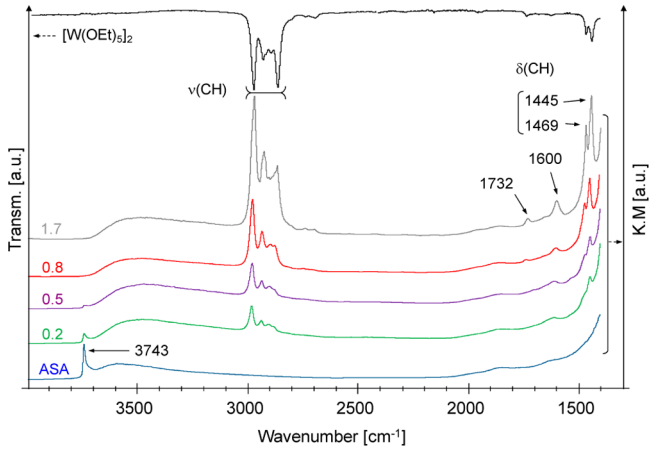

Figure 1. IR spectra (DRIFT) of ASA_{300} and [W(OEt)$_5$]$_2$-IWI-/ASA_{300} materials with increasing W coverage.

vibration band assigned to isolated silanols[44] at 3743 cm^{-1} increasingly disappears and vanishes for coverage above 0.8 W nm^{-2}. Concomitantly, a broad band between 3700 and 3300 cm^{-1} associated with bonded OH appears, in agreement with the presence of residual silanols interacting with organic ligands, probably attached to W, and not accessible to further grafting. Meanwhile, two groups of bands appear in the regions 1800–1450 and 3000–2800 cm^{-1}, assigned to δ(CH) and ν(CH) vibrations of the ethoxy species, respectively. Increasing the tungsten coverage not only increases the ν(CH) and δ(CH) vibration intensity but also leads to the appearance of two additional groups of vibration bands in the 1740–1580 and 1480–1320 cm^{-1} regions: a broad band between 1420 and 1380 cm^{-1} at tungsten coverage below 0.5 W nm^{-2}, and a new band at 1382 cm^{-1} for loading above 0.8 W nm^{-2} (Figure S2, Supporting Information). This band at lower wavenumbers is close to that observed for [W(OEt)$_5$]$_2$ with a δ(CH) at 1374 cm^{-1}. These observations further support the presence of different surface species at low and high W coverage: very likely grafted species at loading below 0.5 W nm^{-2} and then gradually more adsorbed unperturbed [W(OEt)$_5$]$_2$ at higher loadings. In addition, two peaks also appear at ca. 1736 and 1602 cm^{-1} for tungsten coverage above 0.5 W nm^{-2}, which are slightly shifted to 1732 and 1600 cm^{-1}, respectively, at a loading of 1.7 W nm^{-2} and higher. The band at ca. 1736 cm^{-1} is already present in [W(OEt)$_5$]$_2$ and does not shift for carbon-13 labeled compounds, suggesting a combination band related to W–O species. The band at 1600 cm^{-1} likely arises from surface Al–O or Si–O bonds.

The ^{1}H magic angle spinning (MAS) solid-state NMR spectrum of [W(OEt)$_5$]$_2$-IWI-/ASA_{300} prepared with 0.2 W nm^{-2} (Figure 2a) displays four peaks: these at ca. δ 5.0 and 3.7 ppm are tentatively attributed to methylene protons (CH_2) of two different ethoxy species, that at ca. δ 1.0 ppm to methyl protons (CH_3), and that at ca. δ 1.7 ppm to the remaining silanols.[44,45] In addition, the ^{13}C cross-polarization (CP) MAS solid-state NMR spectrum (Figure 2b) displays three peaks:

dx.doi.org/10.1021/cs501311m | ACS Catal. 2014, 4, 4320–4331

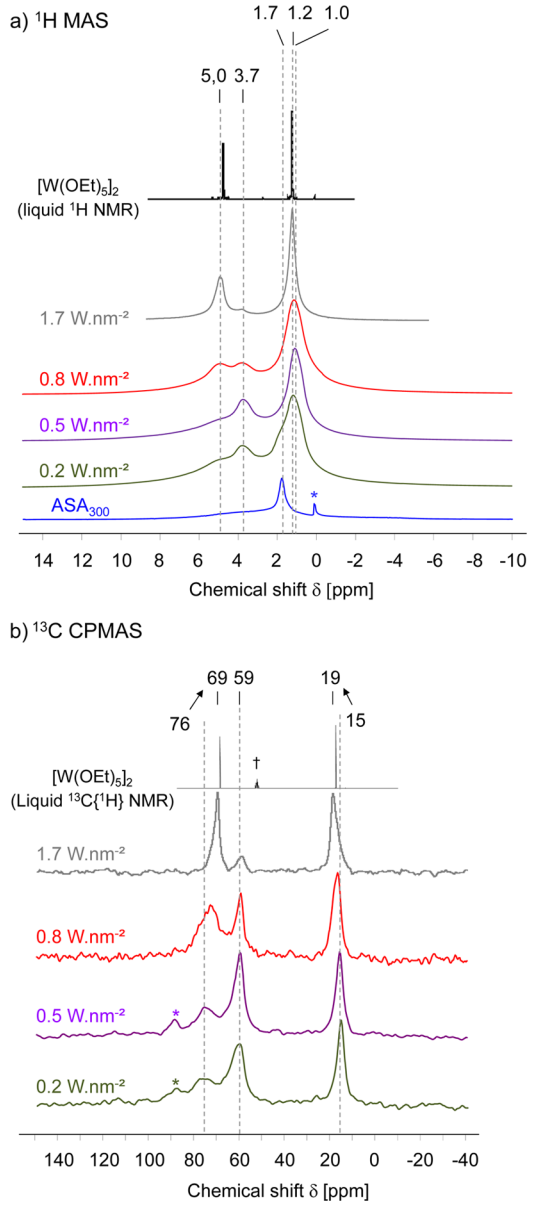

Figure 2. Solid-state NMR spectra of $[W(OEt)_5]_2/ASA_{300}$ materials with increasing W coverage: (a) ^1H MAS spectra; (b) ^{13}C CPMAS spectra. Asterisks denote impurities. ^1H and $^{13}C\{^1H\}$ spectra of $[W(OEt)_5]_2$ are added as references († denotes solvent peak).

one at δ 15 ppm, associated with CH_3 groups, and two at ca. δ 76 and 59 ppm, assigned to two types of OCH_2CH_3 groups, attributed to ethoxy groups bound to W and to the ASA surface, respectively.

Examining the NMR spectra of a series of samples with increasing tungsten loadings is very informative. In the ^1H NMR solid-state spectra (Figure 2a), increasing the tungsten coverage leads to an increase of the intensity of the peak at δ 5.0 ppm as well as a shift of the peak at δ 1.0 ppm to δ 1.2 ppm. Two pairs of peaks are distinguishable and assigned to different types of ethoxy groups: one corresponding to δ 5.0/1.2 ppm and one corresponding to δ 3.7/1.0 ppm, respectively, assigned to ethoxy species linked to W and to ethoxy species chemisorbed on the ASA surface and linked to either Si or Al.

To further quantify surface ethoxides vs ethoxy ligands bound to W, ^1H MAS solid-state NMR spectra were decomposed for materials with coverage varying between ca. 0.2 and 1.7 W nm^{-2} (Figures S3 and S4, Supporting Information) and show that the number of ethoxy ligands bound to each tungsten ($\delta(CH_2)$ 5.0 ppm) is constant and equal to ca. 3.5 ± 0.5 for materials with coverage up to 0.8 ± 0.1 W nm^{-2} (included) and then increases to ca. 4.3 ± 0.5 for higher W coverage. The data are thus consistent with the formation of similar surface species at low W coverage and the presence of additional adsorbed $[W(OEt)_5]_2$ (5 EtO W^{-1}) at higher coverage. Moreover, evaluation of the number of OH groups consumed upon impregnation of $[W(OEt)_5]_2$ shows that the relative percentage of free OH strongly decreases when the W coverage increases from 0.2 to 0.5 W nm^{-2} and it slowly reaches a plateau at higher W coverage (ca. 70 rel % of OH consumed). These results indicate that, above a W coverage of about 0.5–0.8 W nm^{-2}, no more hydroxyls are consumed, consistent with the IR data discussed above. Additional W species must arise from the adsorption of $[W(OEt)_5]_2$, which interact with the first layer of chemisorbed species. The amount of hydroxyls that undergo grafting is associated with their intrinsic reactivity and accessibility linked to the size of the molecular precursor, which prevents the reaction of all OH groups. Of course, the number and reactivity of the hydroxyls involved in the grafting themselves depend on the nature of the support and the type of ASA (surface silica/alumina ratio).

Similarly, the CPMAS ^{13}C solid-state NMR spectrum (Figure 2b) shows that the broad peak at 76 ppm is shifted to 69 ppm at higher W coverage. Its intensity also increases and its line width sharpens. Meanwhile, the peak at 15 ppm is shifted to 19 ppm. As discussed before, chemical shifts observed between 15 and 19 ppm or between 76 and 69 ppm are respectively associated with carbons of CH_3 and OCH_2 groups. Furthermore, a pair of carbons (δ 59/15 ppm) with a high relative intensity is observed at low W coverage. These chemical shifts are similar to these observed for ethoxy species adsorbed on aluminosilicates,[46] revealing that such species are preferentially formed at low W content, when grafting on OH groups happens.

In order to obtain a more detailed understanding of associated surface species structure and relative abundance, ^{13}C-labeled samples at the methylene position were prepared starting from 15–20% labeled molecular precursors denoted $[W(OEt^*)_5]_2$ (see the Supporting Information) and analyzed by ^{13}C MAS and CPMAS solid-state NMR spectroscopy (W coverage ranging from ca. 0.2 to 1.6 W nm^{-2}). Figure 3 shows the ^{13}C MAS solid-state NMR spectra as a function of the W coverage. For a W content of 0.7 W nm^{-2}, only three peaks at ca. 75, 58, and 14 ppm are visible, which are respectively attributed to $[CH_3CH_2\text{-}O\text{-}W\text{-}O_{ASA}]$, $[CH_3CH_2\text{-}O_{ASA}]$, and $[CH_3CH_2\text{-}O\text{-}]$ species. These assignments were confirmed by recording $^1H-^{13}C$ heteronuclear correlation (HETCOR) NMR experiments (Figure S5, Supporting Information).

Above 0.7 W nm^{-2}, sharp peaks appear at 70 and 68 ppm. It is noteworthy that the peak at δ ~75 ppm is very broad and is probably due to a large distribution of chemical shifts, which can be associated with species in different chemical environments. In contrast, above a loading of 0.7 W nm^{-2}, narrower peaks appear, consistent with the presence of species with a more homogeneous environment and probably associated with mobile species. In fact, these sharp signals disappear when recording spectra by cross-polarization techniques (Figure S6, Supporting Information), in agreement with their higher mobility and their assignment to physisorbed species. These

dx.doi.org/10.1021/cs501311m | ACS Catal. 2014, 4, 4320–4331

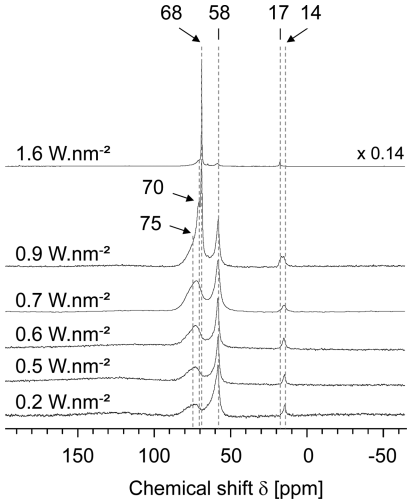

Figure 3. ^{13}C MAS solid-state NMR spectra of ^{13}C-labeled materials supported on ASA, with increasing W coverage.

data confirm the presence of two types of tungsten species: grafted surface species at low tungsten coverage (<0.7 W nm^{-2}, corresponding to a W-bound monolayer) in addition to more mobile species, probably physisorbed on top of the grafted species for higher loadings (>0.8 W nm^{-2}, corresponding to a multilayer).

Note that grafting of $[W(OEt^*)_5]_2$ onto $SiO_{2\text{-}700}$ (0.8 OH nm^{-2}) and $Al_2O_{3\text{-}450}$ (3.5 OH nm^{-2}) leads to materials (0.6 ± 0.1 W nm^{-2}) with IR and NMR signatures similar to those of the corresponding material prepared on ASA (see the Supporting Information for details). However, it is difficult to propose a full assignment of ethoxy ligands bound to specific surface sites belonging to either silica- or alumina-rich material.

In addition, the formation of surface ethoxy groups could occur via two possible scenarios. On the one hand, EtO−M species (M = Si, Al) can directly be formed during the opening of M−O−M′ bridges (M = Si, Al) upon grafting of the W precursor (Scheme 1). On the other hand, since EtOH is also

Scheme 1. Possible Formation of ASA Surface Ethoxy Species, via M−O−M′ Bridge (M = Si, Al) Opening

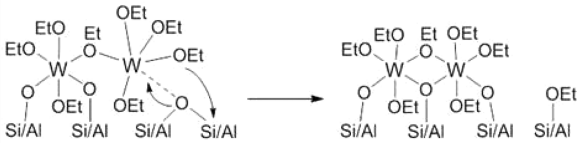

formed during the grafting of a W dimer onto ASA surface OH functionalities, EtOH may subsequently dissociate on the Lewis sites of ASA and form ethoxy species. However, such ethoxy species are only formed to a minor extent.

Sulfidation State of WS_2/ASA Catalysts. Sulfidation of W-based materials were then carried out with a H_2S/H_2 gas mixture for 2 h using various temperatures, and XPS analyses on the sulfide materials were performed to quantify the amount of WS_2 obtained on CSC or conventional catalysts. In particular, their sulfidation level expressed in percentage of WS_2 phase relative to total W species (rel % WS_2), was studied by decomposition of their W 4f spectrum as described in the Supporting Information. Examples of W 4f photopeaks of as-synthesized bulk WS_2, as well as CSC, and calcined catalysts (sulfided at 23 °C, 2 h, 15 mol % H_2S/H_2) are illustrated in Figure 4. Figure 4a reveals first that the molecular compound $[W(OEt)_5]_2$ sulfided at 600 °C in the absence of support (H_2S/H_2, 15 mol % H_2S) easily leads to bulk WS_2 exhibiting ca. 92(±5) rel % WS_2. Then, XPS spectra show that after sulfidation at 23 °C the CSC prepared sample (1.7 W nm^{-2}) obviously contains sulfide species (Figure 4b) while the conventional catalyst (1.8 W nm^{-2}) does not (Figure 4c).

Let us first consider the effect of coverage. When it is sulfided at 350 °C (15 mol % H_2S/H_2), Figure 4d reveals that the CSC WS_2 catalyst with low coverage (0.5 W nm^{-2}) exhibits ca. 76(±5) rel % WS_2 while dried and calcined catalysts only show 51(±5) and 33(±5) rel % WS_2, respectively. These results indicate that the CSC material undergoes an easier sulfidation at low coverage. These differences are less pronounced with high W coverages. Nevertheless, note that the dried catalyst undergoes far better sulfidation than the calcined catalyst, as usually described in the literature,[47] independent of W coverage.

If we now consider a given W coverage of ca. 1.7 W nm^{-2}, sulfidation performed at various temperatures, ranging from −25 to +600 °C, reveals that the rel % WS_2 of conventional catalysts (Figure 4e; see Figure S13 in the Supporting Information for details) follows the well-known S-shaped curves previously reported for conventional calcined NiW/Al_2O_3 catalysts.[14] The level of sulfidation as a function of the applied temperature describes a S-shaped curve with an inflection point located at ca. 350 °C for the calcined sample, close to previously reported data.[14] This inflection point appears at a lower temperature for the dried catalyst, ca. 260 °C. Surprisingly, this inflection point is almost not observed for the CSC catalyst or would be shifted to much lower temperature (around 0 °C). It is noteworthy that CSC materials already reach a good sulfidation level of 50 rel % at room temperature and 30 rel % at −25 °C (Figure 4e), which is unprecedented to the best of our knowledge. This is in sharp contrast with what is known for conventional catalysts, for which the first entities of WS_2 appear only at ca. 150 °C, with the emergence of a partially sulfided phase (noncrystalline oxisulfide intermediate phase) denoted WO_xS_y,[37,48,49] at lower temperature (see Figure S14 in the Supporting Information for a more detailed analysis of the different species). Overall, for catalysts prepared through a molecular approach, sulfidation starts at much lower temperatures.

Morphology and Size Analysis of WS_2/ASA Catalysts. Size analysis of WS_2 slabs was performed by high-resolution transmission electron microscopy (HRTEM) in bright field mode on samples with a W coverage of 1.7−1.8 W nm^{-2}. All TEM data (size and stacking histograms, data analysis) are reported in Table S3 and Figure S15 in the Supporting Information. The main results are illustrated in Figure 5.

For CSC catalysts, the TEM micrographs of Figure 5 reveal the formation of WS_2 layers with increasing length and stacking as the sulfidation temperature increases from −25 to +600 °C. This observation is also consistent with the XPS analysis of the evolution of the W/Al atomic ratio (Figure S12, Supporting Information). At −25 °C (Figure 5a) no WS_2 layers can be detected on CSC catalysts, for which only subnanosized spotlike clusters (ca. 0.5 nm) arranged in nanochain like structures are visible. They are attributed for one part to a noncrystalline oxisulfide phase and for another part to a growing W sulfided phase, as identified by XPS (vide supra, Figure S13, Supporting Information). These entities are the fingerprints of the nucleation and growth mechanisms leading

dx.doi.org/10.1021/cs501311m | ACS Catal. 2014, 4, 4320−4331

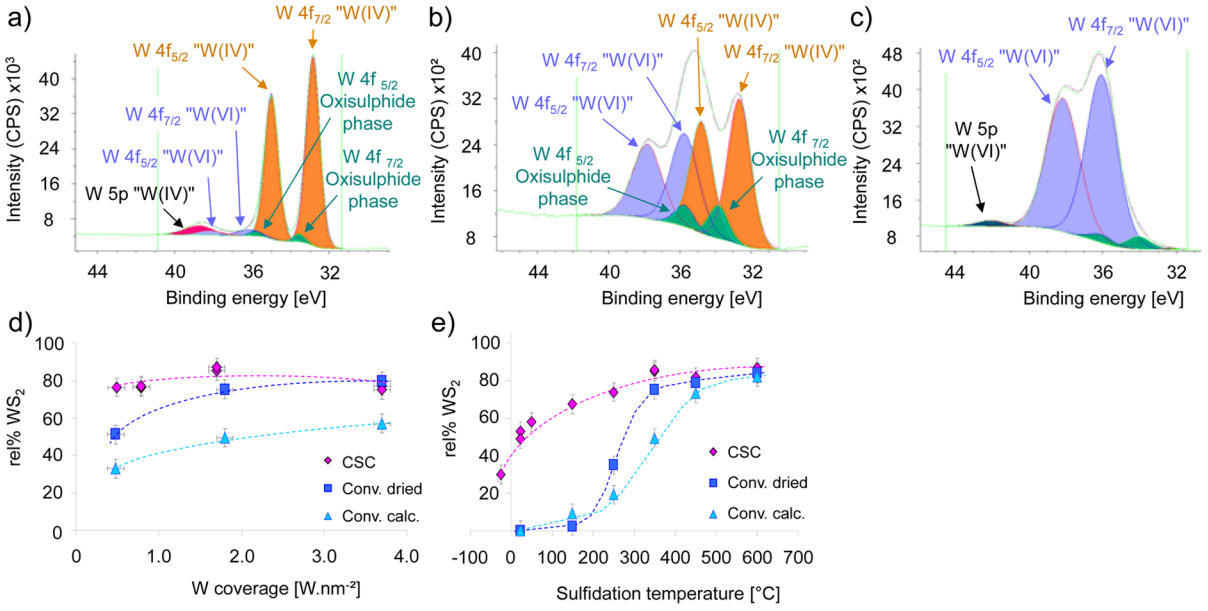

Figure 4. (top) XPS spectra: W 4f photopeaks of (a) bulk WS_2 synthesized by sulfidation (600 °C, see ESI) of $[W(OEt)_5]_2$, (b) CSC (1.7 W nm^{-2}), and (c) conventional calcined (1.8 W nm^{-2}) materials, both sulfided at 23 °C (2 h, 15 mol % H_2S/H_2). (bottom) Relative percentage of W in a WS_2 phase for CSC and conventional catalysts (dried or calcined), as quantified by XPS: (d) sulfided at 350 °C, as a function of the tungsten coverage, and (e) sulfided between 23 and 600 °C (dried or calcined samples) or between −25 and 600 °C (CSC origin) for 2 h, with a 15 mol % H_2S/H_2 mixture, and a W coverage of between 1.7 and 1.8 W nm^{-2}.

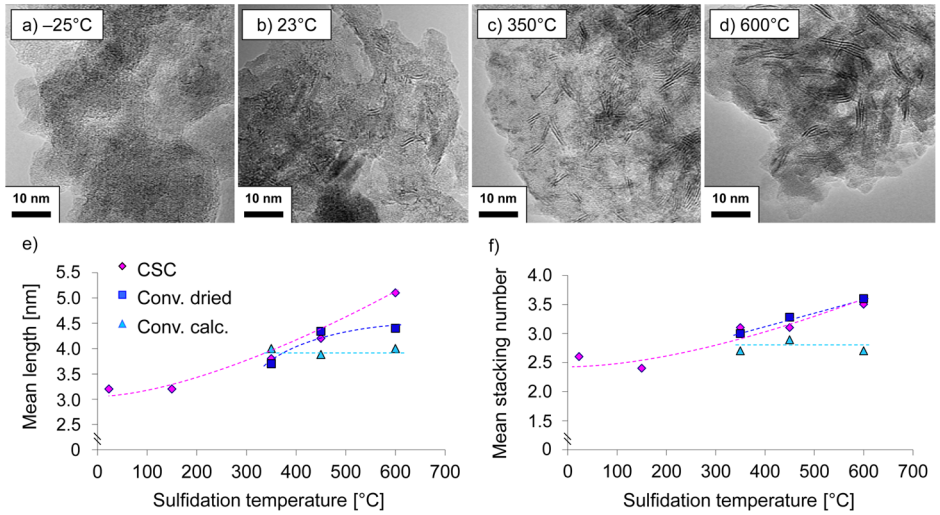

Figure 5. TEM micrographs of WS_2 crystallites observed on CSC catalysts (1.7 W nm^{-2}) sulfided at −25 °C (a), 23 °C (b), 350 °C (c), and 600 °C (d) and TEM size (e) and stacking analysis (f) of WS_2 crystallites (for all catalysts) as a function of the sulfidation temperature (2 h, 15 mol % H_2S/H_2). Tungsten coverage: 1.7−1.8 W nm^{-2}. The uncertainty in the mean length is 15% in (e).

to the final sulfide layers. At 23 °C, the first WS_2 layers of length around 3.2 nm are formed (Figure 5b,e). This result supports the previous XPS analysis and confirms the formation of WS_2 already at ambient temperature.

For CSC and conventional dried catalysts, the mean length of the WS_2 slabs tends to slightly increase when the sulfidation temperature increases (Figure 5e). From 23 to 150 °C, the mean length of CSC catalysts is barely changed at around 3.2 nm, as for the mean stacking number (N), which ranges from 2.6 to 2.4. Between 350 and 600 °C in particular, the mean length (L) changes from ca. 3.8 to 5.1 nm for the CSC catalyst and from 3.7 to 4.4 nm for its conventional counterpart. In the case of the calcined catalysts, no significant change is observed with $L \approx 4.0$ nm. Concerning the stacking number (Figure 5f), CSC and conventional dried catalysts exhibit similar behaviors, with a mean stacking between 3.1 and 3.6. As before, the calcined catalyst does not appear to be sensitive to the sintering effect, as N is constant and equal to ca. 2.7. This weaker sintering effect observed for the calcined sample could arise from stronger interactions between oxide surface species and the ASA support, decreasing the mobility of tungsten atoms and thus preventing nucleation of stacked WS_2 slabs.

Since TEM in bright field mode has certain limitations (observation of only layered W−S sheets oriented with their (001) basal plane along the electron beam direction), high-resolution scanning transmission electron microscopy in high-angle annular dark field mode (HR HAADF-STEM) analyses were performed. In the HAADF-STEM detection mode,

dx.doi.org/10.1021/cs501311m | ACS Catal. 2014, 4, 4320−4331

intensities directly depend on the atomic number Z of the observed atoms. The intensity is proportional to $Z^{1.7}$.[50] HAADF-STEM especially makes it possible to observe WS_2 slabs oriented planar to the surface, enabling the direct detection of their 2D morphology, when they are supported on a model support such as graphite.[51,52] In association with a Cs aberration probe corrector, it is even possible to obtain atom-resolved images of the 2D morphology of conventional WS_2 on an industrial ASA support.[8] Note that, in order to obtain better crystallized slabs, this analysis was undertaken on samples sulfided at 600 °C (in place of 350 °C) and for low W coverage (ca. 0.5 to 0.8 W nm^{-2}). HAADF-STEM micrographs are reported in Figure 6.

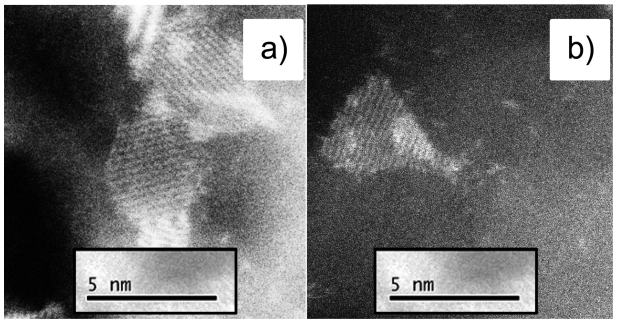

Figure 6. HR HAADF-STEM micrographs of WS_2/ASA catalysts sulfided at 600 °C for 2 h, with 15 mol % H_2S/H_2: (a) CSC catalyst (0.8 W nm^{-2}, this work); (b) conventional catalyst (0.5 W nm^{-2}) according to Girleanu et al.[8]

In Figure 6 representing micrographs of planar WS_2 slabs, CSC and conventional calcined catalysts display different 2D morphologies, revealing the influence of the preparation method. While truncated triangles are observed for conventional WS_2/ASA catalysts (Figure 6b),[8] CSC WS_2 slabs exhibit hexagonal shapes when they are sulfided under the same conditions (T = 600 °C, 2 h, 15 mol % H_2S/H_2; Figure 6a). Note that a similar hexagonal-like morphology is obtained for the CSC catalyst supported on silica (Figure S16, Supporting Information). This result reveals the impact of the preparation method on this 2D shape, and it implies a change of the relative proportion of W-edge and S-edge exhibited by the WS_2 nanocrystallites as rationalized by the following DFT analysis.

Similarly to the MoS_2 system,[53] the morphologies of WS_2 and NiWS conventional catalysts were determined for given sulfo-reductive conditions.[8] For the nonpromoted WS_2 system examined here, the DFT calculations are reported in the Supporting Information to help to quantify the energies of the W-edge and S-edge as a function of the sulfur coverages also controlled by the chemical potential of sulfur in the surrounding gas phase, $\Delta\mu_S$. At T = 600 °C and $p(H_2S)[p(H_2) + p(H_2S)]^{-1} \approx 15\%$ (also used in Figure 6), the chemical potential of sulfur, $\Delta\mu_S$, is estimated to be close to −1.03 eV.[8] The thermodynamically stable morphology calculated from the DFT analysis and Gibbs−Curie−Wulff laws is a truncated triangle exhibiting ca. 60% W-edge (the ratio of edge lengths being $(L_{W\text{-edge}})/(L_{S\text{-edge}})$ = 1.63, Figure 7a,b). In that case, the corresponding sulfur coverages are 87.5% S on the S-edge, and 50% S on the W-edge (Figure 7b). These theoretical results are qualitatively in line with the morphology observed by HAADF-STEM on conventional catalysts sulfided with a 15 mol % H_2S/H_2 mixture (Figure 6b). Obviously these thermodynamic considerations cannot be applied to the CSC catalyst (see also the Discussion).

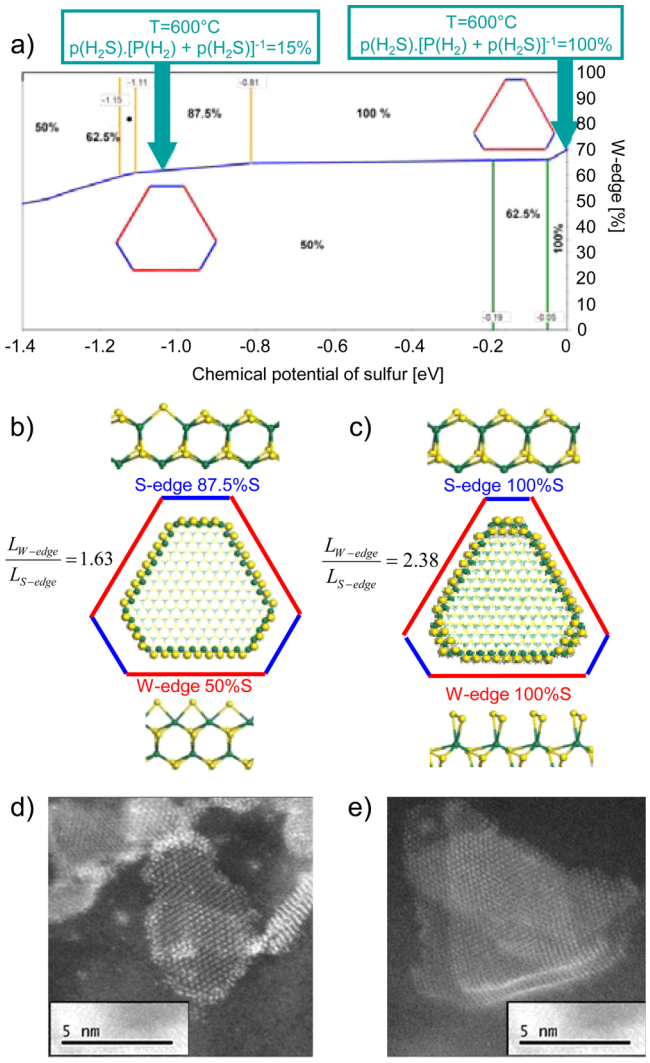

Figure 7. (a) Morphology diagram of WS_2 crystallites as a function of the sulfur chemical potential and the pressure of H_2S, $p(H_2S)[p(H_2) + p(H_2S)]^{-1}$, at 600 °C. The proportion of the W-edge is given by the blue broken line. The percentage of S on the S-edge is reported above the blue line and that on the W-edge composition below this line. (b, c) Atomic structures of the S-edge and W-edge for the conditions T = 600 °C and $p(H_2S)[p(H_2) + p(H_2S)]^{-1}$ = 15% (b) or pure H_2S (c).

Let us now consider the effect of the sulfo-reductive conditions on the resulting morphology of WS_2 given by the Gibbs−Curie−Wulff laws. According to the DFT calculations, in pure H_2S ($\Delta\mu_S \approx 0$), the sulfur coverages at the edges increase to 100% S on both M- and S-edges and the morphology should exhibit a higher proportion of W-edge: ca. 71% ($L_{W\text{-edge}}/L_{S\text{-edge}}$ = 2.38, as represented in Figure 7c). To further investigate this effect, we have tested two harsher sulfidation conditions. The first one uses a longer period of sulfidation (30 h) under 15 mol % H_2S/H_2 at 600 °C. After this treatment, WS_2 crystallites adopt more truncated triangular shapes (Figure 7d), as predicted by theoretical models under thermodynamic conditions (Figure 7a,b), although larger and more stacked slabs are observed as a result of sintering under these conditions. The second set of conditions with sulfidation at T = 600 °C under pure H_2S (2 h) yields WS_2 crystallites with a more triangular shape (Figure 7e). This trend is consistent

dx.doi.org/10.1021/cs501311m | ACS Catal. 2014, 4, 4320−4331

with the equilibrium morphology predicted by DFT (Figure 7a,c) and will be discussed later on.

Toluene Hydrogenation Catalytic Activities. Catalytic results obtained for samples with increasing W coverages sulfided at 350 °C (2 h, 15 mol % H_2S/H_2) prior to the catalytic test were normalized per mole of W (r_i; see Figure S17a, Supporting Information) or per mole of W engaged in the active WS_2 phase (r_i'; see Figure S17b, Supporting Information). They reveal that, when the W coverage is increased from 0.5 to 3.7 W nm^{-2}, the intrinsic HYD rate is greater for CSC catalysts (0.33 mol of tol (mol of W_{WS_2})$^{-1}$ h^{-1}, with 1.7 W nm^{-2}) than for conventional dried (0.23 mol of tol (mol of W_{WS_2})$^{-1}$ h^{-1}, with 1.8 W nm^{-2}) and in particular calcined catalysts (0.14 mol of tol (mol of W_{WS_2})$^{-1}$ h^{-1}, with 1.8 W nm^{-2}).

For an optimal coverage of 1.7−1.8 W nm^{-2}, increasing the sulfidation temperature from 350 to 600 °C gives similar results, as shown in Figure 8 (r_i') and Figure S18 (r_i): CSC catalysts exhibit a higher intrinsic HYD rate (r_i') than conventional and calcined catalysts, whatever the sulfidation temperature. In addition, increasing the sulfidation temperature decreases r_i'. This effect, which is more easily observed for CSC samples, is correlated with the sintering of WS_2 slabs for high sulfidation temperatures, as previously evidenced by TEM (see Figure 5).

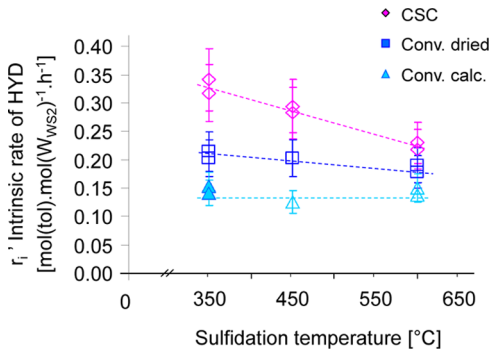

Figure 8. Intrinsic rates of toluene hydrogenation of CSC and conventional catalysts (coverage 1.7−1.8 W nm^{-2}) sulfided at 350, 450, and 600 °C prior to catalytic tests (2 h, 15 mol % H_2S/H_2): (filled symbols) spent catalysts which underwent XPS analyses; (empty symbols) spent catalysts for which previously high rel % WS_2 values have been supposed to be similar before and after testing (as observed for samples with 3.7 W nm^{-2}; not shown).

Overall, for the standard sulfidation temperature of 350 °C, HYD performances (r_i') of CSC catalysts are significantly improved in comparison with both dried and conventional calcined catalysts, making the understanding of the effect of the preparation method on the size or the morphology of WS_2 an important step of this study.

DISCUSSION

Nature of Surface Species. Upon deposition of $[W(OEt)_5]_2$ onto ASA, the molecular complex undergoes grafting through the reaction with surface OH groups. At low W coverage (<0.8(±0.1) W nm^{-2}), spectroscopic investigations have revealed the presence of grafted tungsten ethoxy species and surface ethoxy directly linked to Si and/or Al of ASA. The grafted W surface species contain an average of 3.5(±0.5) ethoxy ligands per W. Grafting of $[W(OEt)_5]_2$ on related silica and alumina supports indicate that M−O−M′ bridges (M = Al, Si) are probably involved in the reaction between the molecular complex and the surface, consistent with the formation of surface ethoxy species. The observation of NMR signals and the absence of any EPR signal speak for the conservation of the dinuclear structure of the W(V) complex on the surface.

At this point, four families of surface species can be proposed, corresponding to different ethoxy W^{-1} ratios: monografted dinuclear species (4.5 EtO W^{-1}), bis-grafted dinuclear species (4.0 EtO W^{-1}), tris-grafted dinuclear species (3.5 EtO W^{-1}) and tetrakis-grafted dinuclear species (3.0 EtO W^{-1}). The formation of bis-grafted species is in line with the high density of surface OH in ASA_{300} (3.2 OH nm^{-2}). For comparison, grafting a molecular precursor on $SiO_{2\text{-}200}$ (2.8 OH nm^{-2}) leads mainly to bis-grafted species.[21,29a,54,55] The surface species are thus probably dinuclear species, having an average of seven remaining ethoxy ligands, and being attached by three bonds to the ASA surface; an idealized average structure is represented in Figure 9a. Finally, considering that the surface OH density is 3.2 OH nm^{-2} and that the maximum density of tungsten centers is 2.0 W nm^{-2}, the formation of grafted species at low W coverage is expected to proceed via grafting on surface OH groups but also through the opening of adjacent M−O−M′ bridges (M = Si, Al; M′ = Si, Al).[55c]

For tungsten coverage above 0.8 (±0.1) W nm^{-2}, additional tungsten species are present, with IR and NMR spectroscopic signatures very close to that of $[W(OEt)_5]_2$. In view of the saturation of the surface with grafted species, these species probably correspond to adsorbed $[W(OEt)_5]_2$ weakly interacting with the grafted layer via either W−O(Et)−W bridges or weaker electrostatic interactions (Figure 9b). In fact, washing the material with cyclohexane decreases the coverage from 1.7 to 1.4 W nm^{-2}. In addition, this proposal is consistent with the increased number of EtO ligands bound to W from 3.5 to

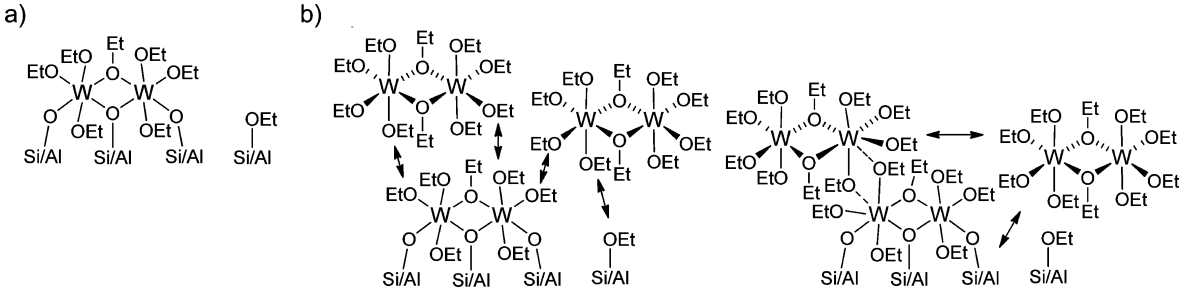

Figure 9. Example of tungsten surface species probably found on $[W(OEt)_5]_2$-based material at (a) low W coverage and (b) high W coverage. Black arrows indicate electrostatic interactions.

dx.doi.org/10.1021/cs501311m | ACS Catal. 2014, 4, 4320−4331

4.3(±0.5) at a loading greater than 0.8 W nm^{-2}, a value closer to the expected number for $[W(OEt)_5]_2$.

Finally, it must be underlined that no Al extraction was observed in the CSC sample, in contrast to what is observed for conventional preparation methods using heptamolybdate[9] or heptatungstate[56] precursors in solution. In addition, no mixed phase such as $[AlW_6]$[9,56] or hydrotalcite type phase[10] is observed. The better control of chemical interaction between the grafted W complex and the ASA support in non aqueous medium avoids these unwanted phenomena occurring with conventional methods of preparation. This impacts the observed sulfidation levels and morphology effects as discussed hereafter.

Origin of the Higher Sulfidation Level of CSC Catalysts. During sulfidation, the amount of WS_2 formed is expected to depend mainly on the number and type of surface species and the strength of W−O bonds of the ancillary or the surface ligands, here W−OEt and M−O−W (M = Al, Si), respectively. Since the sulfidation process also corresponds to the reduction of the metallic species, we undertook complementary H_2-TPR experiments (Figure S19, Supporting Information), which showed that CSC surface species are quantitatively and more easily reduced. In fact, "W−OEt" bonds in $[W(OEt)_5]_2$ are rather labile, which favors ligand exchange[57] and facilitates the reaction between $[W(OEt)_5]_2$-based surface species and H_2S/H_2. For example, sulfidation of the molecular compound $[W(OEt)_5]_2$ at 600 °C (H_2S/H_2,15 mol % H_2S) led to bulk WS_2 exhibiting ca. 92(±5) rel % WS_2 (Figure 4a). In contrast, conventional polyoxometalate precursors (used in conventional materials) exhibit stronger cohesive energies which require higher energy to cleave "W−O" bonds and "depolymerize" $[WO_4]^{2-}$ tungsten clusters. In addition, for calcined materials, amorphous WO_3 is formed as refractory species to sulfidation because of even stronger cohesive energies. The temperature of calcination of conventional samples is also well-known to affect the final sulfidation degree of the catalyst.[15]

When tungsten loading is increased, W species form a grafted monolayer plus additional layers in CSC catalysts vs stacked WO_x species in conventional materials. These weakly bound layers behave like pure $[W(OEt)_5]_2$, thus facilitating sulfidation, in comparison with stacked WO_x species. It is thus not surprising to find that the highest level of sulfidation of supported W materials prepared with $[W(OEt)_5]_2$ is close to 92(±5) rel % of the amount of tungsten detected by XPS.

Morphology Effects Sensitive to the Preparation Method and Sulfidation Treatment. According to the HAADF-STEM and DFT results, there is a clear difference in the 2D morphology of WS_2 obtained by CSC (hexagon) vs conventional preparation methods (truncated triangle) for 15 mol % H_2S/H_2 sulfidation conditions, as shown in Figure 6. In particular, the observed morphology for the CSC sample does not correspond to what is expected from thermodynamics for 15 mol % H_2S/H_2 sulfidation conditions according to calculations, while it does under the more severe pure H_2S sulfidation conditions (Figure 7), thus showing that controlling the morphology requires milder preparation methods. The fact that increasing the sulfidation time (30 h instead of 2 h) under the milder 15 mol % H_2S/H_2 sulfidation conditions also allows the equilibrium state (truncated triangle) to be reached suggests that the CSC preparation method involves specific kinetic effects which enable the formation of a metastable morphology, closer to a hexagon under milder conditions. Such differences in morphology induce a change in the distribution of W-edge and S-edge sites around the crystallites, possibly affecting the catalytic activity of WS_2.

Impact of Size and Morphology on TOF. Toluene HYD activity was renormalized with respect to the amount of edge atoms per slab, taken as potential active sites, without distinguishing the specific activity of S-edge, W-edge, and corner sites, whose structures are shown in Figure 7b). Calculations were performed by taking into account the size and morphology analyses of WS_2 slabs as previously proposed (see the Supporting Information for numerical details)[58] assuming hexagonal and truncated triangle models for CSC and conventional catalysts, respectively.

The turnover frequency (TOF) of HYD, r_i'', expressed in mol of tol (mol of edge site)$^{-1}$ h^{-1}, is reported in Figure 10 for samples sulfided at 350, 450, and 600 °C prior to catalytic testing.

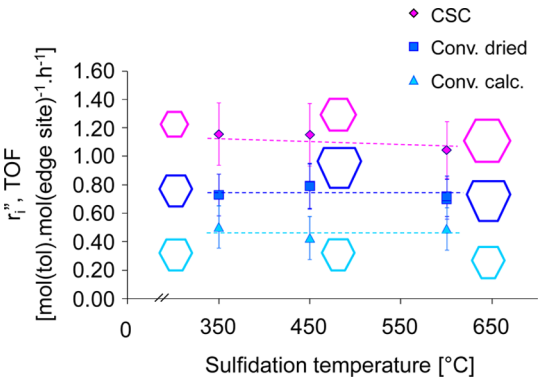

Figure 10. Toluene hydrogenation TOF (r_i'') of CSC and conventional catalysts as a function of the sulfidation temperature. Tungsten coverage: ca. 1.7−1.8 W nm^{-2}. Corresponding "as supposed" WS_2 morphologies are provided.

First, the TOF values are rather constant whatever the sulfidation temperature for each catalyst, indicating that the normalization of toluene hydrogenation intrinsic rates by the amount of edge active sites enables a correct account of size effects. This point is particularly relevant for CSC catalysts, for which WS_2 slab sizes evolve from 3.8 to 5.1 nm as a function of the sulfidation temperature. The CSC catalysts display TOF values 40% higher than those for conventional catalysts. Assuming that the 2D morphology of CSC catalysts could be even more triangular (as truncated triangular slabs reflect the most thermodynamically stable geometry from DFT calculations), calculations of TOF values using truncated triangular shapes for CSC samples were performed, and these values were found to be barely different from these discussed above. As a consequence, this analysis highlights the different intrinsic quality of active sites exposed for CSC catalysts.

Another possibility is that the "quality" of the sites is modulated by the stacking number. TEM studies revealed that, between 350 and 600 °C, calcined catalysts are slightly less stacked (2.7−2.9) than CSC (3.1−3.5) and/or dried species (3.0−3.6). Although this difference is rather marginal, one can wonder if this might play a role. Considering the "rim-edge" model established on MoS_2 single crystals,[59] HYD sites would be located predominantly on the top and bottom of edge planes, so-called "rim" sites. Thus, WS_2 slabs exhibiting low stacking numbers would be more efficient, as they would

dx.doi.org/10.1021/cs501311m | ACS Catal. 2014, 4, 4320−4331

maximize their number of rim sites. Note that a similar reasoning should hold true for "brim" sites[60] located on the basal plane of WS_2 slabs.[61] However, the calcined catalyst exhibiting the lowest stacking is the least hydrogenating. Therefore, "rim-edge" and "brim" models do not seem to be linked with the observed TOF. Note that the "rim-edge" model was proposed on MoS_2 single crystals with a significantly higher stacking number, which is not the case here.

Therefore, the difference in TOF probably arises from another factor: i.e., the different 2D morphologies between conventional and CSC catalysts observed by HAADF-STEM analysis (Figure 6). Considering DFT calculations (Figure 7), WS_2 crystallites close to experimental sulfidation conditions exhibit W-edge with a sulfur coverage of 50% (i.e., 50% of S atoms have been removed from the bulk reference state), while the S-edge exhibits a sulfur coverage of 87.5% (i.e., 12.5% of coordinatively unsaturated sites (CUS)[62]). The local atomic structures of W sites are given in Figure 7b and thus differ qualitatively between the S-edge and W-edge. If we refer to MoS_2 phases,[63] it appears that hydrogen species such as MSH and MH species can be stabilized on both edges, resulting from the dissociation of H_2 on Mo sites and/or MoS sites. Activation energies for H_2 dissociation and the lability of H species involved in hydrogenation steps of toluene are expected to differ from one edge to the other. In addition, previous kinetic modeling studies of toluene hydrogenation[64] have shown that the maximum TOF in toluene hydrogenation is obtained when the optimal coverages of adsorbed toluene and MSH species are reached. The simultaneous presence of these two types of edge sites in a hexagonal structure is thus expected to favor both H_2 activation and toluene activation while minimizing the competition between the two steps for the same sites. Hence, the higher activity of CSC catalysts is attributed to the hexagonal shape of their crystallites (observed by HAADF-STEM), providing an optimal distribution of edge sites required for toluene adsorption and H_2 activation.

CONCLUSION

A controlled synthesis of ASA-supported WS_2 HDT catalysts with a molecular level characterization, by combining experiment and theory, not only allows a detailed understanding of the influence of each of the synthetic elementary steps[65] on the final structure of the catalyst but also provides an improved catalytic activity (hydrogenation) in comparison with conventional catalysts. The two-step preparation method involves a grafting/deposition of a molecular precursor, $[W(OEt)_5]_2$, on ASA partially dehydroxylated at 300 °C and a sulfidation (2 h, 15 mol % H_2S/H_2) to yield WS_2 slabs with hexagonal morphologies, in place of the truncated triangular morphologies of conventional catalysts.

The optimal catalyst has a 1.7(±0.1) W nm^{-2} coverage, for which the first step ("grafting/deposition") yields grafted dinuclear W species as well as a layer of physisorbed $[W(OEt)_5]_2$. At coverage below 0.8(±0.1) W nm^{-2}, the reaction of $[W(OEt)_5]_2$ on ASA_{300} yields selectively grafted dinuclear species, having an average of seven remaining ethoxy ligands and attached by three bonds to the ASA surface. This multiple grafting is accompanied by the formation of ethoxy groups linked to the ASA surface, a process probably assisted by W. At higher tungsten coverage (above 0.8(±0.1) W nm^{-2}), additional tungsten species are physisorbed in a layer interacting with grafted dinuclear surface species via weak interactions. Adsorbed and grafted species keep their molecular character and display significantly "weaker" interactions with the support or adjacent W than in the conventionally prepared catalysts.

This first step has a dramatic impact on the temperature and level of sulfidation as well as on the WS_2 morphology according to XPS, TEM, HAADF-STEM, and DFT analyses and on the toluene hydrogenation catalytic activity. First, CSC catalysts require much milder sulfidation conditions, which occurs at temperatures as low as −25 °C and reach an unprecedented level of sulfidation (50 rel %) at ambient temperature, which has never been observed for conventional catalysts. At higher temperature, highly sulfided samples are obtained, with sulfidation level ranging from 76 to 85(±5) rel % WS_2 from 0.5 to 3.7 W nm^{-2}, exceeding what is observed for their conventional counterparts. In addition, this approach yields hexagonal 2D morphology in place of the truncated triangular phase observed for the conventional catalysts. To the best of our knowledge such a 2D morphology evolution induced by the preparation method has never been reported.

Evaluation of the rate per WS_2 edge sites (TOF) further highlights the higher activity of the CSC catalysts, sulfided between 350 and 600 °C, especially for the species with a 1.7 W nm^{-2} coverage. The hexagonal morphology of CSC catalysts (sulfided at 600 °C) probably provides a more favorable edge structure, with a synergy effect between W-edge and S-edge, as supported by DFT modeling. This synergy effect could enhance H_2 activation into MSH and MH species as well as toluene activation when adsorbed on the crystallite edges. The precise origin of the distinct 2D morphology is attributed to kinetic effects driven by the preparation method. Overall, this molecular approach provides clues about the genesis of supported WS_2 phases and a structure−reactivity relationship in HDT catalysts. Given the promising and improved activity of this nonpromoted HDT catalyst, we are currently working on further improving catalyst formation and preparation methods for unpromoted as well as Ni(Co)-promoted materials.

ASSOCIATED CONTENT

Supporting Information

The following files are available free of charge on the ACS Publications website at DOI: 10.1021/cs501311m.

Syntheses, additional IR and NMR spectra, XPS details, NMR spectra decomposition process, TEM and HAADF-STEM data, WS_2 slab 2D models, and further details (PDF)

AUTHOR INFORMATION

Corresponding Authors

*E-mail for C.C.: ccoperet@inorg.chem.ethz.ch.
*E-mail for P.R.: pascal.raybaud@ifpen.fr.

Notes

The authors declare no competing financial interest.

ACKNOWLEDGMENTS

The authors thank M. Cartes (ETH) and F. Héroguel (ETH) for silica-based materials, M. Valla (ETH) and M. G. Vidalie (IFPEN) for NMR experiments, L. Lemaitre (IFPEN) for IR analyses, and P. Lecour (IFPEN) for XPS analyses.

REFERENCES

(1) Commission Regulation (EU) No 459/2012 of 29 May 2012 amending Regulation (EC) No 715/2007 of the European Parliament

and of the Council and Commission Regulation (EC) No 692/2008 as regards emissions from light passenger and commercial vehicles (Euro 6).
(2) Kibsgaard, J.; Lauritsen, J. V.; Lægsgaard, E.; Clausen, B. S.; Topsøe, H.; Besenbacher, F. *J. Am. Chem. Soc.* **2006**, *128*, 13950−13958.
(3) *Catalysis by transition metal sulfides*; Raybaud, P., Toulhoat, H., Eds.; Technip: Paris, 2013; p 248.
(4) Topsøe, H.; Clausen, B. S.; Candia, R.; Wivel, C.; Mørup, S. *J. Catal.* **1981**, *68*, 433−452.
(5) Raybaud, P.; Hafner, J.; Kresse, G.; Kasztelan, S.; Toulhoat, H. *J. Catal.* **2000**, *190*, 128−143.
(6) Drescher, T.; Niefind, F.; Bensch, W.; Grünert, W. *J. Am. Chem. Soc.* **2012**, *134*, 18896−18899.
(7) Stanislaus, A.; Cooper, B. H. *Catal. Rev.: Sci. Eng.* **1994**, *36*, 75−123.
(8) Girleanu, M.; Alphazan, T.; Boudene, Z.; Bonduelle-Skrzypczak, A.; Legens, C.; Gay, A. S.; Copéret, C.; Ersen, O.; Raybaud, P. *ChemCatChem* **2014**, *6*, 1594−1598.
(9) Carrier, X.; Lambert, J. F.; Che, M. *J. Am. Chem. Soc.* **1997**, *119*, 10137−10146.
(10) Delacaillerie, J. B. D.; Kermarec, M.; Clause, O. *J. Am. Chem. Soc.* **1995**, *117*, 11471−11481.
(11) Bergwerff, J. A.; Visser, T.; Leliveld, B. R. G.; Rossenaar, B. D.; De Jong, K. P.; Weckhuysen, B. M. *J. Am. Chem. Soc.* **2004**, *126*, 14548−14556.
(12) Costa, D.; Arrouvel, C.; Breysse, M.; Toulhoat, H.; Raybaud, P. *J. Catal.* **2007**, *246*, 325−343.
(13) Shimada, H. *Catal. Today* **2003**, *86*, 17−29.
(14) Breysse, M.; Cattenot, M.; Decamp, T.; Frety, R.; Gachet, C.; Lacroix, M.; Leclercq, C.; de Mourgues, L.; Portefaix, J. L.; Vrinat, M.; Houari, M.; Grimblot, J.; Kasztelan, S.; Bonnelle, J. P.; Housni, S.; Bachelier, J.; Duchet, J. C. *Catal. Today* **1988**, *4*, 39−55.
(15) Hensen, E. J. M.; van der Meer, Y.; van Veen, J. A. R.; Niemantsverdriet, J. W. *Appl. Catal., A* **2007**, *322*, 16−32.
(16) Bonduelle-Skrzypczak, A.; Legens, C. In *Catalysis by transition metal sulfides*; Raybaud, P., Toulhoat, H., Eds.; Technip: Paris, 2013; pp 247−258.
(17) Chizallet, C.; Raybaud, P. *Angew. Chem., Int. Ed.* **2009**, *48*, 2891−2893.
(18) (a) Yermakov, Y. I.; Kuznetsov, B. N. *Kinet. Katal.* **1972**, *13*, 1355−1356. (b) Yermakov, Y. I. *Stud. Surf. Sci. Catal.* **1981**, *7*, 57−76.
(19) Ballard, D. G. H. *Adv. Catal.* **1973**, *23*, 263−275.
(20) Basset, J. M.; Choplin, A. *J. Mol. Catal.* **1983**, *21*, 95−108.
(21) Copéret, C.; Chabanas, M.; Petroff Saint-Arroman, R.; Basset, J. M. *Angew. Chem., Int. Ed.* **2003**, *42*, 156−181.
(22) Wegener, S. L.; Marks, T. J.; Stair, P. C. *Acc. Chem. Res.* **2012**, *45*, 206−214.
(23) (a) Thomas, J. M. *Angew. Chem., Int. Ed.* **1999**, *38*, 3588−3628. (b) Jarupatrakorn, J.; Tilley, T. D. *J. Am. Chem. Soc.* **2002**, *124*, 8380−8388. (c) Mania, P.; Verel, R.; Jenny, F.; Hammond, C.; Hermans, I. *Chem. - Eur. J.* **2013**, *19*, 9849−9858.
(24) Marks, T. J. *Acc. Chem. Res.* **1992**, *25*, 57−65.
(25) Joubert, J.; Delbecq, F.; Sautet, P.; Le Roux, E.; Taoufik, M.; Thieuleux, C.; Blanc, F.; Copéret, C.; Thivolle-Cazat, J.; Basset, J. M. *J. Am. Chem. Soc.* **2006**, *128*, 9157−9169.
(26) Delgado, M.; Santini, C. C.; Delbecq, F.; Wischert, R.; Le Guennic, B.; Tosin, G.; Spitz, R.; Basset, J. M.; Sautet, P. *J. Phys. Chem. C* **2010**, *114*, 18516−18528.
(27) (a) Conley, M. P.; Delley, M. F.; Siddiqi, G.; Lapadula, G.; Norsic, S.; Monteil, V.; Safanova, O. V.; Copéret, C. *Angew. Chem., Int. Ed.* **2014**, *53*, 1872−1876. (b) Delley, M. F.; Nunez-Zarur, F.; Conley, M. P.; Comas-Vives, A.; Siddiqi, G.; Norsic, S.; Monteil, V.; Safonova, O. V.; Copéret, C. *Proc. Natl. Acad. Sci. U.S.A* **2014**, *111*, 11624−11629.
(28) Blanc, F.; Berthoud, R.; Salameh, A.; Basset, J. M.; Copéret, C.; Singh, R.; Schrock, R. R. *J. Am. Chem. Soc.* **2007**, *129*, 8434−8435.
(29) (a) Rhers, B.; Salameh, A.; Baudouin, A.; Quadrelli, E. A.; Taoufik, M.; Copéret, C.; Lefebvre, F.; Basset, J. M.; Solans-Monfort, X.; Eisenstein, O.; Lukens, W. W.; Lopez, L. P. H.; Sinha, A.; Schrock, R. R. *Organometallics* **2006**, *25*, 3554−3557. (b) Mazoyer, E.; Merle, N.; de Mallmann, A.; Basset, J. M.; Berrier, E.; Delevoye, L.; Paul, J. F.; Nicholas, C. P.; Gauvin, R. M.; Taoufik, M. *Chem. Commun.* **2010**, *46*, 8944−8946. (c) Conley, M. P.; Mougel, V.; Peryshkov, D. V.; Forrest, W. P.; Gajan, D.; Lesage, A.; Emsley, L.; Copéret, C.; Schrock, R. R. *J. Am. Chem. Soc.* **2013**, *135*, 19068−19070.
(30) (a) Chabanas, M.; Baudouin, A.; Copéret, C.; Basset, J. M. *J. Am. Chem. Soc.* **2001**, *123*, 2062−2063. (b) Salameh, A.; Joubert, J.; Lukens, W.; Baudouin, A.; Delbecque, F.; Sautet, P.; Basset, J. M.; Copéret, C. *Angew. Chem., Int. Ed.* **2007**, *46*, 3870−3873.
(31) (a) Le Roux, E.; Taoufik, M.; Copéret, C.; de Mallmann, A.; Thivolle-Cazat, J.; Basset, J. M.; Maunders, B. M.; Sunley, G. J. *Angew. Chem., Int. Ed.* **2005**, *44*, 6755−6758. (b) Le Roux, E.; Taoufik, M.; Baudouin, A.; Copéret, C.; Thivolle-Cazat, J.; Basset, J. M.; Maunders, B. M.; Sunley, G. J. *Adv. Synth. Catal.* **2007**, *349*, 231−237. (c) Basset, J. M.; Copéret, C.; Soulivong, D.; Taoufik, M.; Thivolle-Cazat, J. *Acc. Chem. Res.* **2010**, *43*, 323−334. (d) Samantaray, M. K.; Callens, E.; Abou-Hamad, E.; Rossini, A. J.; Widdifield, C. M.; Dey, R.; Emsley, L.; Basset, J. M. *J. Am. Chem. Soc.* **2014**, *136*, 1054−1061.
(32) (a) Yermakov, Y. I.; Kuznetsov, B. N.; Startsev, A. N.; Zhdan, P. A.; Shepelin, A. P.; Zaikovskii, V. I.; Plyasova, L. M.; Burmistrov, V. A. *J. Mol. Catal.* **1981**, *11*, 205−214. (b) Yermakov, Y. I.; Startsev, A. N.; Burmistrov, V. A. *Appl. Catal.* **1984**, *11*, 1−13.
(33) Thomas, T. J.; Brenner, A. *J. Mol. Catal.* **1983**, *18*, 197−202.
(34) Maugé, F.; Vallet, A.; Bachelier, J.; Duchet, J. C.; Lavalley, J. C. *Catal. Lett.* **1989**, *2*, 57−61.
(35) Halbert, T. R.; Ho, T. C.; Stiefel, E. I.; Chianelli, R. R.; Daage, M. *J. Catal.* **1991**, *130*, 116−129.
(36) Choi, J. S.; Maugé, F.; Pichon, C.; Olivier-Fourcade, J.; Jumas, J. C.; Petit-Clair, C.; Uzio, D. *Appl. Catal., A* **2004**, *267*, 203−216.
(37) Okamoto, Y.; Kato, A.; Usman; Rinaldi, N.; Fujikawa, T.; Koshika, H.; Hiromitsu, I.; Kubota, T. *J. Catal.* **2009**, *265*, 216−228.
(38) Roukoss, C.; Laurenti, D.; Devers, E.; Marchand, K.; Massin, L.; Vrinat, M. *C. R. Chim.* **2009**, *12*, 683−691.
(39) Ben Tayeb, K.; Lamonier, C.; Lancelot, C.; Fournier, M.; Payen, E.; Bonduelle, A.; Bertoncini, F. *Catal. Today* **2010**, *150*, 207−212.
(40) Perdew, J. P.; Chevary, J. A.; Vosko, S. H.; Jackson, K. A.; Pederson, M. R.; Singh, D. J.; Fiolhais, C. *Phys. Rev. B* **1992**, *46*, 6671−6687.
(41) Kresse, G.; Furthmuller, J. *Comput. Mater. Sci.* **1996**, *6*, 15−50.
(42) Kohn, W.; Sham, L. J. *Phys. Rev.* **1965**, *140*, A1133−A1138.
(43) Kresse, G.; Joubert, D. *Phys. Rev. B* **1999**, *59*, 1758−1775.
(44) *The Surface Properties of Silicas*; Legrand, A. P., Ed.; Wiley: Chichester, U.K., 1998.
(45) Brunner, E. *Catal. Today* **1997**, *38*, 361−376.
(46) Derouane, E. G.; Nagy, J. B.; Dejaifve, P.; van Hooff, J. H. C.; Spekman, B. P.; Vedrine, J. C.; Naccache, C. *J. Catal.* **1978**, *53*, 40−55.
(47) Reinhoudt, H. R.; van der Meer, Y.; van der Kraan, A. M.; van Langeveld, A. D.; Moulijn, J. A. *Fuel Process. Technol.* **1999**, *61*, 43−54.
(48) (a) Kooyman, P. J.; Hensen, E. J. M.; de Jong, A. M.; Niemantsverdriet, J. W.; van Veen, J. A. R. *Catal. Lett.* **2001**, *74*, 49−53. (b) Reinhoudt, H. R.; van Langeveld, A. D.; Kooyman, P. J.; Stockman, R. M.; Prins, R.; Zandbergen, H. W.; Moulijn, J. A. *J. Catal.* **1998**, *179*, 443−450.
(49) Gandubert, A. D.; Krebs, E.; Legens, C.; Costa, D.; Guillaume, D.; Raybaud, P. *Catal. Today* **2008**, *130*, 149−159.
(50) Nellist, P. D.; Pennycook, S. J. *Science* **1996**, *274*, 413−415.
(51) Hansen, L. P.; Ramasse, Q. M.; Kisielowski, C.; Brorson, M.; Johnson, E.; Topsøe, H.; Helveg, S. *Angew. Chem., Int. Ed.* **2011**, *50*, 10153−10156.
(52) (a) Carlsson, A.; Brorson, M.; Topsøe, H. *J. Microsc.* **2006**, *223*, 179−181. (b) Brorson, M.; Carlsson, A.; Topsøe, H. *Catal. Today* **2007**, *123*, 31−36.
(53) Schweiger, H.; Raybaud, P.; Toulhoat, H. *J. Catal.* **2002**, *212*, 33−38.
(54) (a) Lefort, L.; Chabanas, M.; Maury, O.; Meunier, D.; Copéret, C.; Thivolle-Cazat, J.; Basset, J. M. *J. Organomet. Chem.* **2000**, *593*−*594*, 96−100. (b) Le Roux, E.; Taoufik, M.; Chabanas, M.; Alcor,

D.; Baudouin, A.; Copéret, C.; Thivolle-Cazat, J.; Basset, J. M.; Lesage, A.; Hediger, S.; Emsley, L. *Organometallics* **2005**, *24*, 4274−4279.
(55) (a) Bouh, A. O.; Rice, G. L.; Scott, S. L. *J. Am. Chem. Soc.* **1999**, *121*, 7201−7210. (b) Ajjou, J. A. N.; Rice, G. L.; Scott, S. L. *J. Am. Chem. Soc.* **1998**, *120*, 13436−13443. (c) Demmelmaier, C. A.; White, R. E.; van Bokhoven, J. A.; Scott, S. L. *J. Phys. Chem. C* **2008**, *112*, 6439−6449.
(56) Carrier, X.; Lambert, J. F.; Che, M. *Stud. Surf. Sci. Catal.* **1998**, *118*, 469−476.
(57) *The chemistry of metal alkoxides*; Turova, N. Y., Turevskaya, E. P., Kessler, V. G., Yanovskaya, M. I., Eds.; Kluwer Academic: London, 2002.
(58) Kasztelan, S.; Toulhoat, H.; Grimblot, J.; Bonnelle, J. P. *Appl. Catal.* **1984**, *13*, 127−159.
(59) Daage, M.; Chianelli, R. R. *J. Catal.* **1994**, *149*, 414−427.
(60) Topsøe, H.; Hinnemann, B.; Nørskov, J. K.; Lauritsen, J. V.; Besenbacher, F.; Hansen, P. L.; Hytoft, G.; Egeberg, R. G.; Knudsen, K. G. *Catal. Today* **2005**, *107−108*, 12−22.
(61) Füchtbauer, H. G.; Tuxen, A. K.; Moses, P. G.; Topsøe, H.; Besenbacher, F.; Lauritsen, J. V. *Phys. Chem. Chem. Phys.* **2013**, *15*, 15971−15980.
(62) Siegel, S. *J. Catal.* **1973**, *30*, 139−145.
(63) Prodhomme, P. Y.; Raybaud, P.; Toulhoat, H. *J. Catal.* **2011**, *280*, 178−195.
(64) (a) Guernalec, N.; Cseri, T.; Raybaud, P.; Geantet, C.; Vrinat, M. *Catal. Today* **2004**, *98*, 61−66. (b) Guernalec, N.; Geantet, C.; Raybaud, P.; Cseri, T.; Aouine, M.; Vrinat, M. *Oil Gas Sci. Technol.* **2006**, *61*, 515−525.
(65) *Synthesis of Solid Catalysts*; de Jong, K. P., Ed.; Wiley-VCH: Weinheim, Germany, 2009.